Supporting Information

The Effect of Sulfurization Reaction Rate with Sulphur Concentration Gradient dependence on the Growth Pattern and Morphological Evolution of MoS_2 in Laminar Flow

Zhen-Hua Han[a,†], Qi-Bo Wang[a,†], Qin-Qin Xu[a,*], Xin-Hui Qiu[b], Tong Cheng[a], Dong-Sheng Jiao[a] and Jian-Zhong Yin[a]

a: *State Key Laboratory of Fine Chemicals, School of Chemical Engineering, Dalian University of Technology, 2 Ling Gong Road, 116024, Dalian, China*

b: *The Second Hospital of Dalian Medical University, 467 Zhong Shan Road, 116021, Dalian, China*

† These authors contributed equally to this work and should be considered co-first authors.

* *Corresponding author e-mail:* qinqinxu@dlut.edu.cn

Table of Contents

i. Effect of supersaturation on precursor particle size

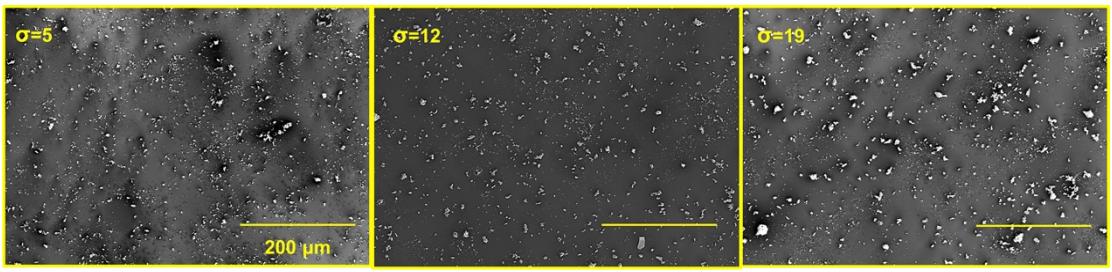

Figure. S1 SEM image of precursor particles on the substrate surface at different σ.

Calculation of σ:

The value of σ is obtained by weighing the target amount of $MoO_2(acac)_2$ and dissolving it in a high-pressure dissolution reactor. The calculation method for the amount of reagent required at different σ is as follows:

In our previous study, the solubility of Mo in $scCO_2$ is determined by static method at different dissolution parameters[1]. The solubility of $MoO_2(acac)_2$ in $scCO_2$ could be determined by the following equation:

$$S = \frac{M_1 \cdot y_1 \cdot \rho_2}{M_2 \cdot (1 - y_1)} \tag{1}$$

In the formula, M_1 and M_2 correspond to the relative molecular masses of the solute and solvent, respectively, and y1 is the mole fraction of the solute.

CO_2 did not have solvent capable below the critical point (T≈31.4 °C, p≈7.4 MPa), so to quantitatively describe the degree of supersaturation of the precursor, supersaturation, σ_c, is redefined as follows[2]:

$$\sigma_c = \frac{S_1}{S_c} \tag{2}$$

Where, S_1 is the solubility of the solute at initial pressure, and S_c represents the solubility at the critical point.

The dissolution vessel used in this experiment has a volume V of approximately 178 ml. Based on equation (1~2) and combined with our previous research work[1,2], the required solute masses at 50 °C and 20 MPa, for σ_c of 5, 12, and 19, are calculated to be 0.169 g, 0.406 g, and 0.642 g, respectively.

ii. Effect of substrate pretreatment on contact angle and MoS_2 growth

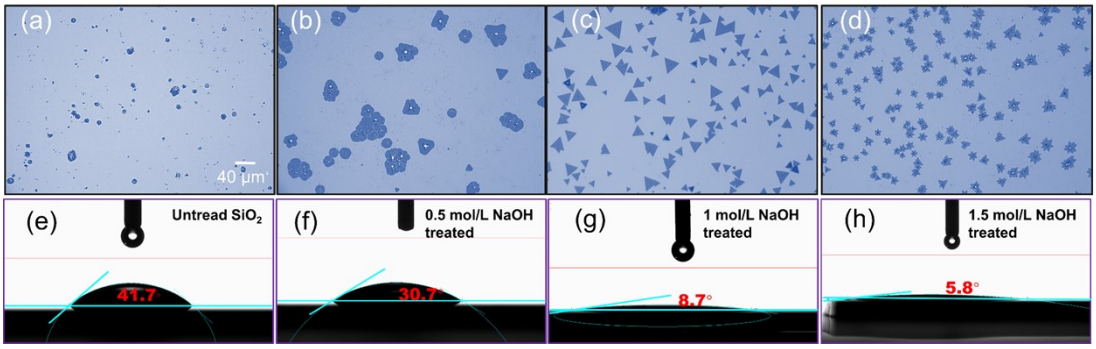

Figure S2 Contact angle and MoS_2 growth OM images of the substrate surface before and after NaOH solution treatment.

As shown in Figure S2(a)-(d), after pretreatment, the MoS_2 morphology shifts from "edge-blunted triangular" to "sharp-edged ortho-triangular" to "polygonal star shape" but when the substrate is untreated, insignificant growth is found. With increasing concentration, the contact angle decreases from 41.7° to 5.8° as shown in Figure S2(e)~(h). The contact angle shows a negative correlation with the wetting area of the particles after melting. The large wetting area leads to excessively high growth rates under sulfur-sufficient conditions. This leads to thermodynamically stable growth of multilayer structures at grain boundaries or monolayer MoS_2. Therefore, a suitable concentration of NaOH solution can provide favorable support for subsequent high-quality and uniform growth.

iii. Effect of sulfuration parameters on the MoS_2 growth

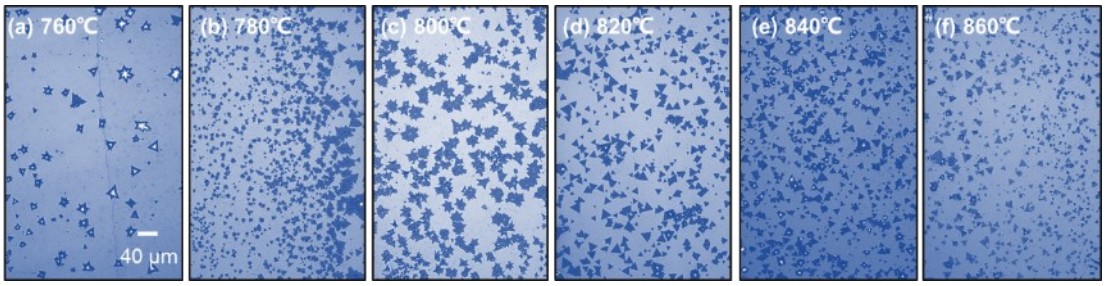

Figure S3. OM images of MoS_2 growth at 760 °C~860 °C.

The effect of growth temperature on MoS_2 morphology is explored. As shown in Figure S3(a)~(f), the thickness changes from multilayer to monolayer and then to multilayer as the temperature increases. And the domain size first increases, then decreases and finally stabilizes. Precursor diffusion rate and particle melting degree increase with growth temperature[3,4]. A low diffusion rate at low temperatures reduces the rate of crystal growth, and tends to grow vertically on unmelted particles (with a low nucleation energy barrier). The increase in temperature led to a more complete melting of the particles. The MoS_2 size increased and tended to grow in monolayers as the growth rate increased. However, too high growth temperature leads to excessive growth rate, causing MoS_2 to transition from monolayer to multilayer. In addition, high temperature degrades the grown MoS_2 edges and reduces the film quality[5]. Therefore, 820 °C is used as a control variable for MoS_2 growth.

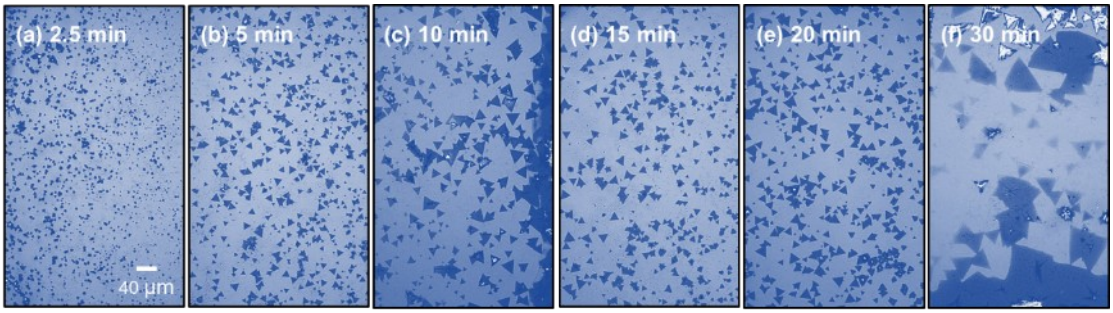

Figure S4. MoS_2 OM images of the substrate surface at different growth times.

Figure S4(a)~(g) shows the OM images of MoS_2 at different growth times. With the increase of growth time, the domain size tends to increase and the nucleation density decreases gradually. At 2.5 min, the presence of small-sized MoS_2 (~10 μm) suggests that sulfuration has started before 2.5 min. As the growth time increases, the liquid phase precursor also melts more completely and more sulfur vapor is involved in sulfuration, which leads to a significant increase in size. However, when the growth time is too long, it leads to a transition from isolated MoS_2 to large continuous films. And there exists degradation caused by too long time as shown in Figure S4(f). In addition, shorter or longer growth time result in vertical growth of MoS_2. The former leads to incomplete melting of the particles and inadequate sulfuration. The latter results in lateral growth to a critical size and then continues to grow in multilayers above. Therefore, 20 min is chosen as the optimal growth time.

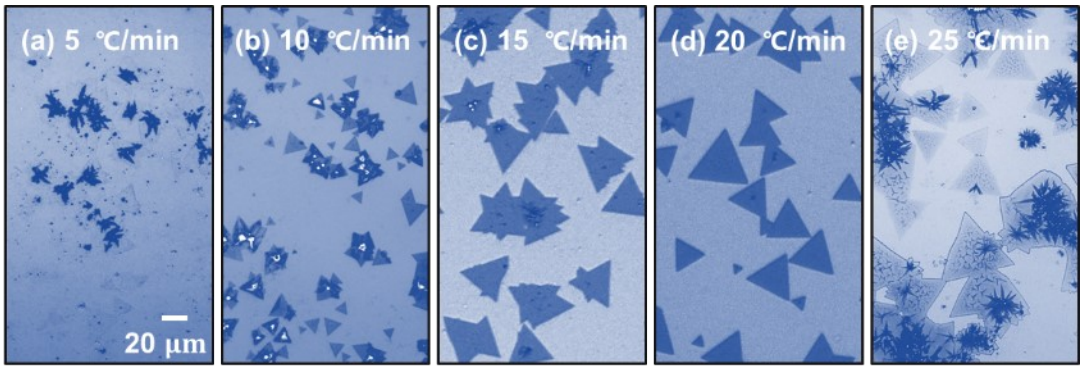

Figure S5. MoS_2 OM images at different temperature rise rates.

The OM images of MoS_2 grown at different heating rates are shown in Figure S5(a)~(f). With the increase of heating rates, the MoS_2 domain size shows an enlarging trend with the number of layers transformation from multilayer to monolayer, and the morphology of the domain area is gradually transformed into a regular triangle with sharp edges. Increasing of heating rates means the particles melting time of the particles is shortened, leading to an increase in the rate of Mo source supply, which makes the growth rate progressively more suitable for monolayer MoS_2 with large size, while lower growth rates lead to vertical growth[2]. Consequently, the appropriate rate ensures that the S:Mo ratio is relatively stable, growing sharp-edged triangles. Furthermore, the growth of dendritic MoS_2 occurs at 5 °C/min and 25 °C/min as shown in Figure S5(a) and (e), and the size is relatively large at high rates. Growth defects are caused by high reaction rates due to the high temperature gradient. And the lower heating rate makes the Mo source supply rate slower, resulting in a relatively excessive sulfur concentration atmosphere. This leads to the appearance of dendritic morphology[6]. In summary, the optimal growth temperature, growth time and temperature rise rate are 820 °C, 20 min, and 20 °C/min, respectively.

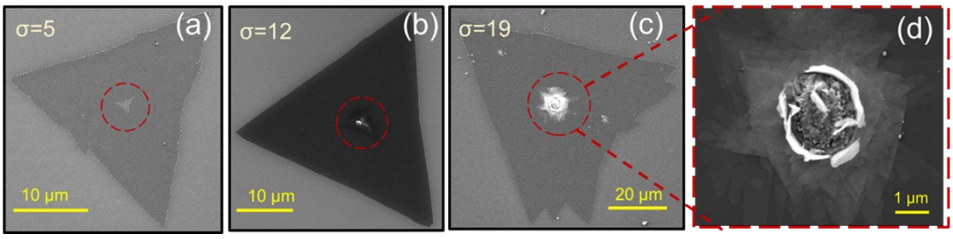

Figure S6. (a)~(c) are SEM images of MoS_2 at σ of 5, 12, and 19, respectively. (d) Magnified image of the area circled in red in Figure (c).

iv. Uniform growth of MoS_2 within laminar boundary layers

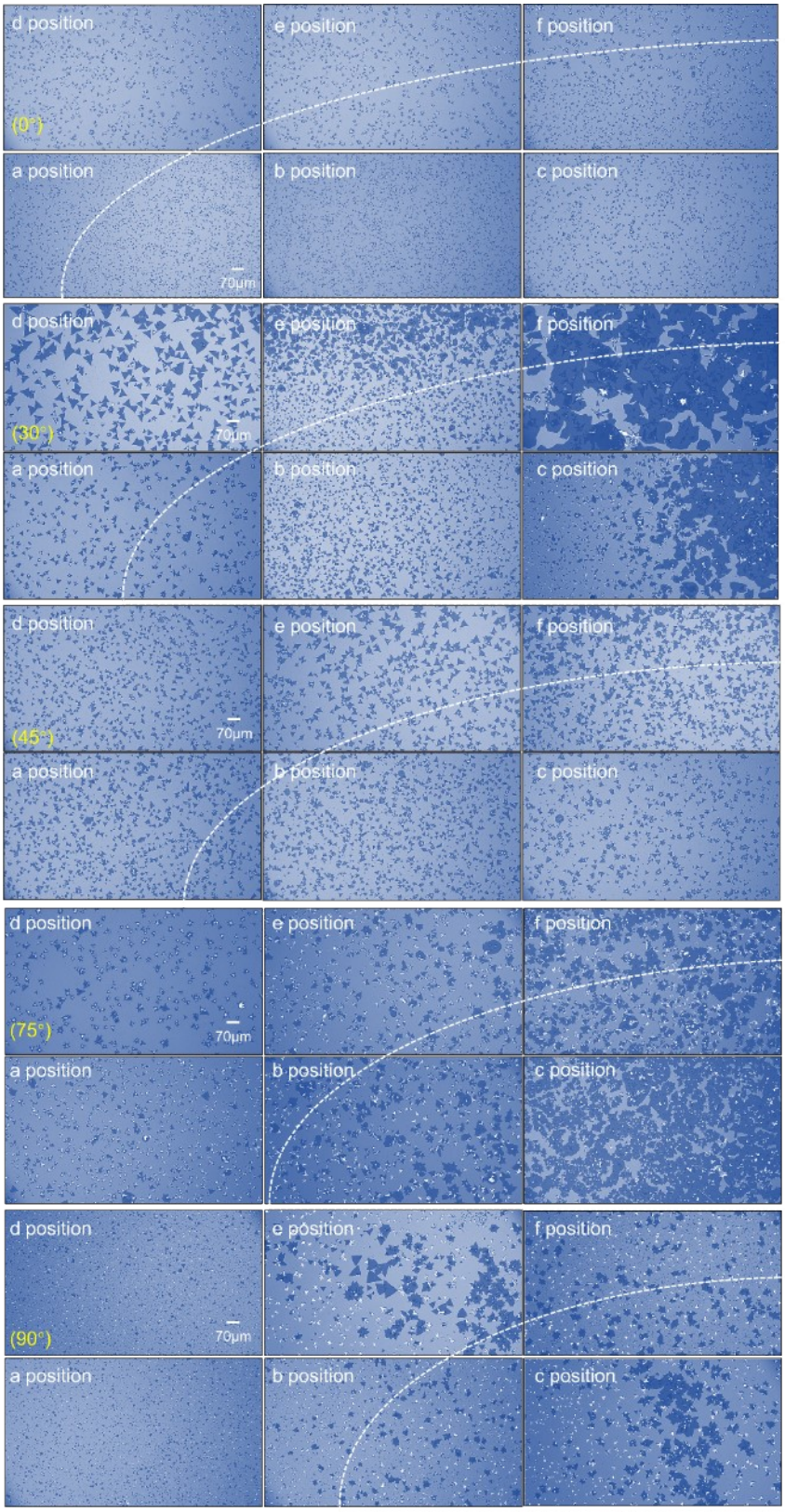

Figure S7. MoS_2 OM images at different positions of the substrate (a~f) at different θ (with FPG) in ULB model.

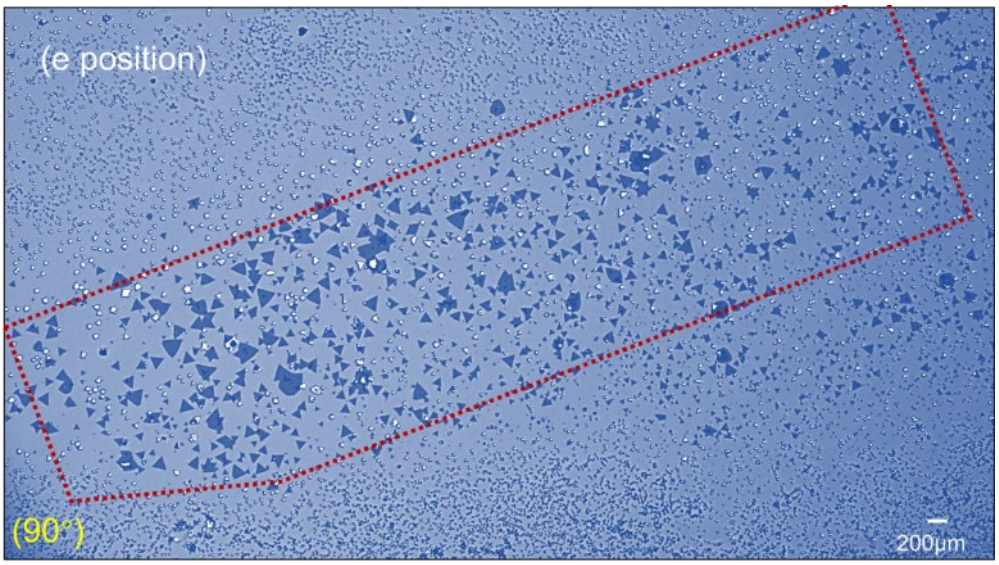

Figure S8. shows the OM image of MoS_2 grown at the slit formed between the quartz boat and the substrate (position marked by the red rectangular dashed line) at θ=90°.

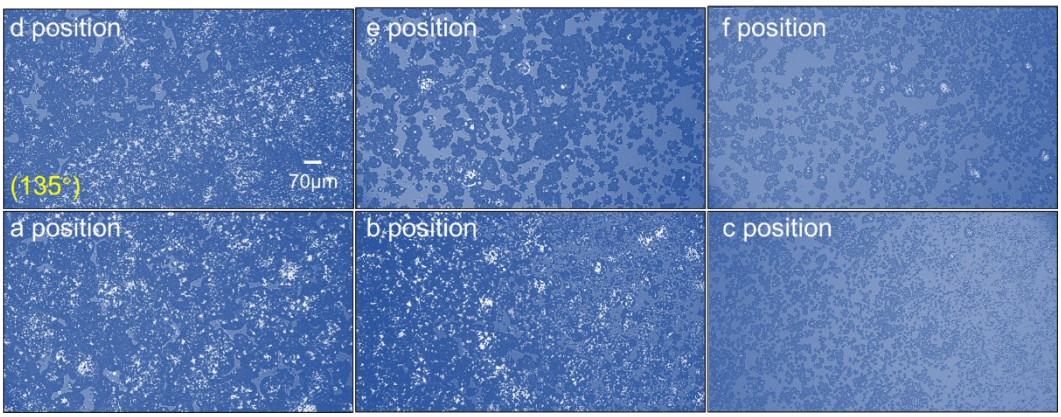

Figure S9. MoS_2 OM images of different positions (a~f) of the substrate at θ=135° (with APG) in ULB model.

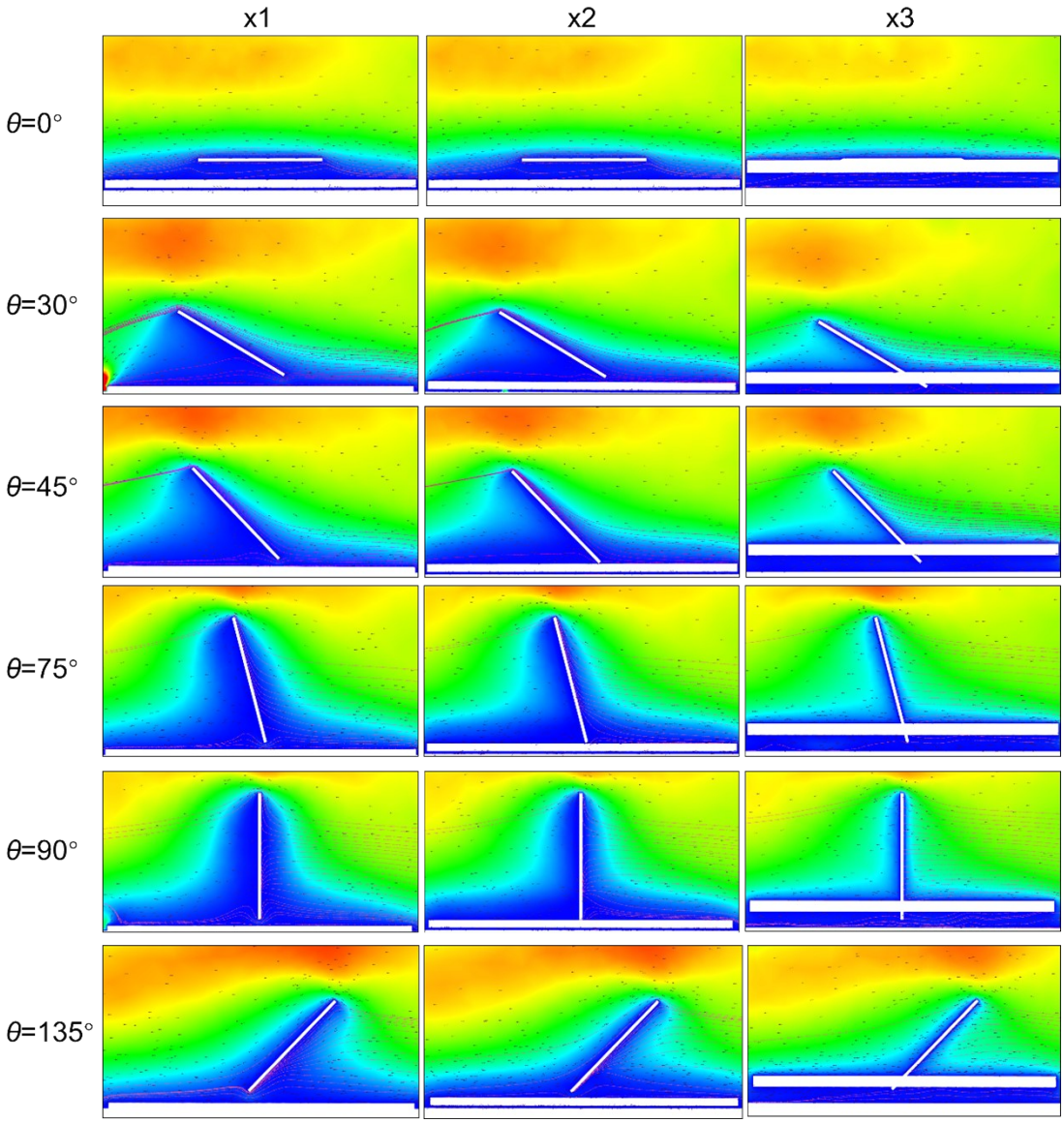

Figure S10. Simulation results of boundary layer thickness development (at different θ) for different cross sections from x1 to x3 in the ULB model.

v. Uniform growth of MoS_2 within laminar flow

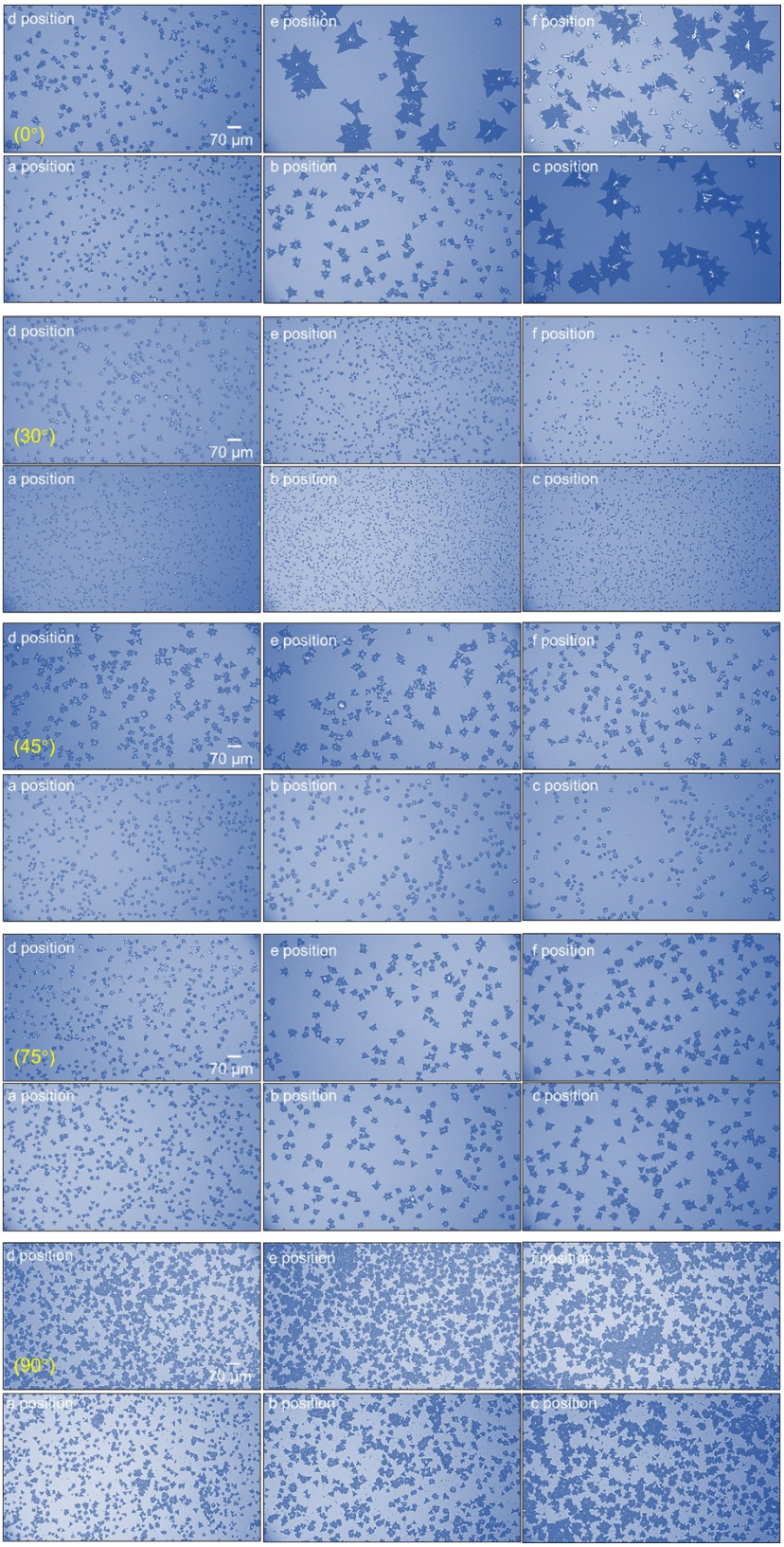

Figure S11. MoS_2 OM images of different positions (a~f) of the substrate at θ=0°~90° in FDL model.

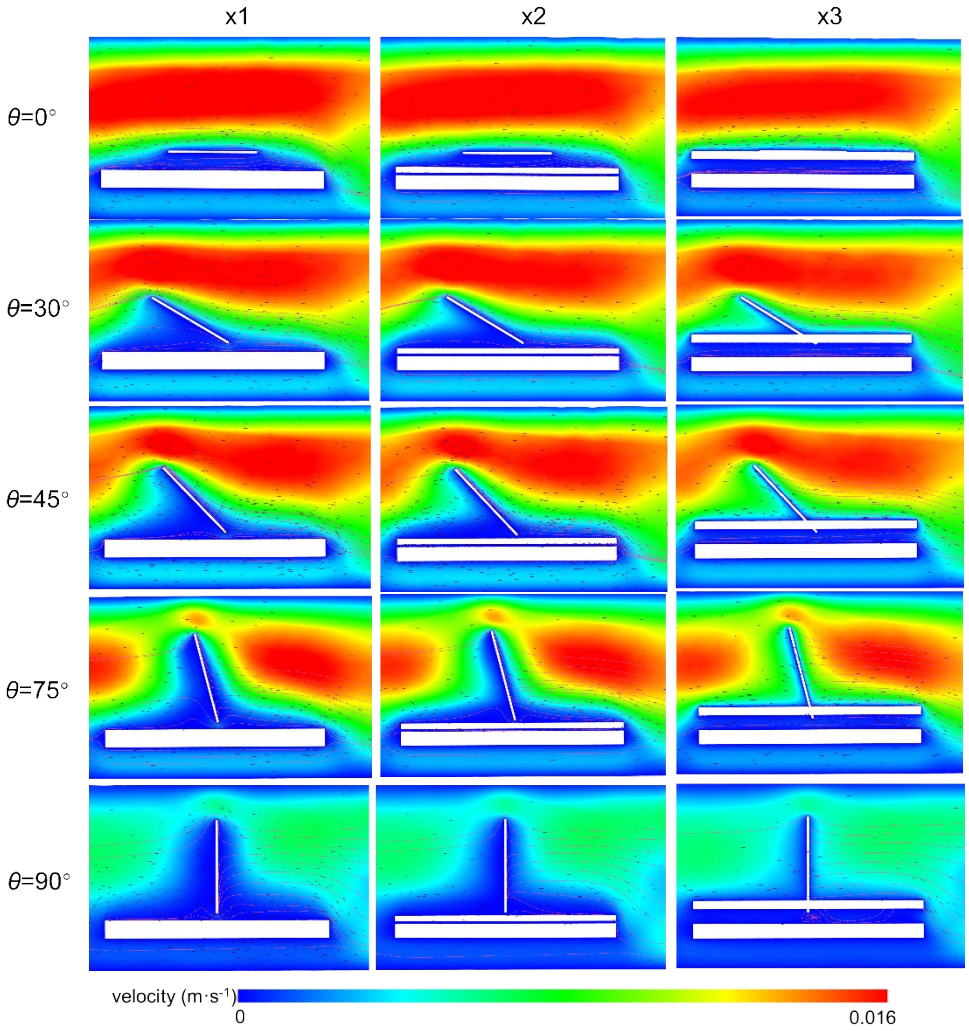

Figure S12. Simulation results of boundary layer thickness development (θ=0°~90°) for different cross sections from x1 to x3 in the FDL model.

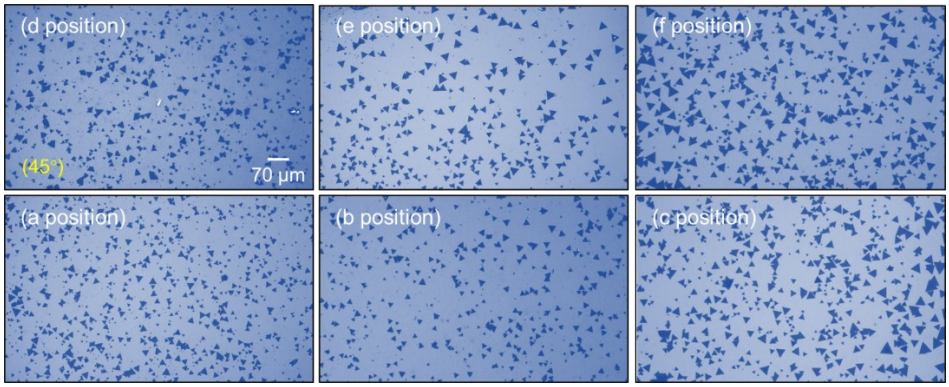

Figure S13. OM image of WS_2 in ULB model, θ=45° condition.

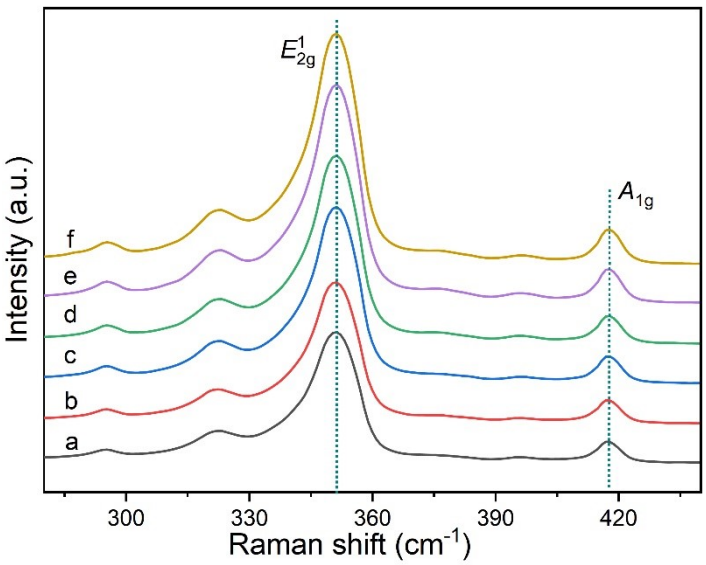

Figure S14. Raman spectra of monolayer WS_2 grown at different positions within the ULB with θ=45°.

vi. CFD simulation calculation details

To quantitatively demonstrate that the underdeveloped boundary layer growth model is more conducive to controlled, high-quality, and uniform growth, we have computed the component transport coefficients (H_g), chemical reaction coefficients (K_0), and crystal growth rates (g). This allows for a more quantitative inference of the characteristics of the ULB and FDL growth models.

The diffusion coefficients of the gas mixtures form the basis for solving the parameters. The diffusion coefficients of binary components are obtained using the multicomponent model. Binary gas diffusion coefficients can be derived from molecular theory by considering two gases (ij) and solving the Boltzmann equation to obtain the diffusion coefficient D_{ij} between them.

$$D_{i,j} = \frac{0.00266T^{\frac{3}{2}}}{PM_{ij}^{\frac{1}{2}}\eta_{ij}^{2}\Omega_D} \tag{3}$$

$$\Omega_D = \frac{A}{(T^*)^B} + \frac{C}{exp(DT^*)} + \frac{E}{exp(FT^*)} + \frac{G}{exp(HT^*)} \tag{4}$$

where, $T^*=kT/\varepsilon_{ij}$，$\varepsilon_{ij}=(\varepsilon_i\varepsilon_j)^{1/2}$, A=1.06036，B=0.15610，C=0.19300，D=0.47635, E=1.03587，F=1.52996，G=1.76474，H=3.89411.

The equation is applicable for low to moderate pressures, where $M_{ij}^{1/2}=2[(1/M_i)+(1/M_j)]^{-1}$ where M_i and M_j are the molecular weights of components i and j, respectively. η_{ij} is the characteristic length in the intermolecular force equation, and Ω_D is the collision integral, which is a function of temperature. The characteristic energy (ε) and characteristic length (η) are specifically provided in Table 1. According to the experimental growth temperature (820 ℃) and pressure (101325 Pa), the binary gas diffusion coefficients D_{ij} for each gas component can be theoretically calculated using the binary diffusion formula as 1.26×10^{-5} (m^2/s).

During the CVD growth process, there are two fluxes:1) The flux of precursors transported from the main gas stream through the boundary layer to the substrate surface, which is expressed as:

$$F_{mass-transport} = H_g(C_g - C_0) \tag{5}$$

2) The amount consumed by the precursor participating in the chemical reaction on the substrate surface can be expressed as:

$$F_{surface-reaction} = K_0 C_0 \tag{6}$$

where H_g represents the mass transport coefficient, K_0 is the surface reaction constant, C_g represents the molar concentration of precursor in the mainstream (kmol/m^3), and C_0 represents the molar concentration of precursor on the substrate surface.

At steady state, $F_{\text{mass-transport}}$=$F_{\text{surface-reaction}}$.

$$C_0 = \frac{1}{1 + {K_0}/{H_g}} C_g \tag{7}$$

Where H_g can be estimated from the obtained gas diffusion coefficient D_g.

$$H_g = \frac{D_g}{\delta} \quad \text{……} \qquad \text{……(8)}$$

Subsequently, the molar concentrations of precursors in the mainstream and on the substrate surface are obtained from the simulation results and then substituted into the above equation to calculate the H_g and K_0 values for both ULB and FDL growth models, as shown in Table S2 and Table S3.

Table S1. Specific characteristic energies (ε) and characteristic lengths (η) for each component.

	Ar	S(gas)
η(Å)	3.542	4.035
ε/k(K)	93.3	137.9

Table S2. H_g and K_0 values for the ULB growth model.

θ	δ_1	δ_2	*Hg*-1	*Ks*-1	*Hg*-2	*Ks*-2
0°	0.64	0.61	0.197	1.158	0.207	0.604
30°	1.61	0.35	0.078	0.406	0.361	1.240
45°	1.88	0.28	0.067	0.318	0.451	1.958
75°	2.23	0.71	0.057	0.225	0.178	0.666
90°	3.01	0.86	0.042	0.163	0.147	0.509

Table S3. H_g and K_0 values for the FDL growth model.

θ	δ_1	δ_2	*Hg*-1	*Ks*-1	*Hg*-2	*Ks*-2
0°	0.60	0.59	0.210	0.022	0.214	0.040
30°	1.01	0.29	0.125	0.0179	0.435	0.029
45°	1.25	0.25	0.101	0.0126	0.505	0.074
75°	1.49	0.51	0.085	0.0060	0.247	0.022
90°	3.13	0.87	0.043	0.0009	0.145	0.005

Reynolds number calculation:

The viscosity coefficient of the mixed gas is determined using the ideal-gas-mixing-law model. The specific formula is as follow：

$$\mu = \sum_i \frac{X_i \mu_i}{\sum_j X_j \Phi_{ij}} \tag{9}$$

$$\Phi_{ij} = \frac{[1 + \left(\frac{\mu_i}{\mu_j}\right)^{\frac{1}{2}} (\frac{M_{w,j}}{M_{w,i}})^{1/4}]^2}{[8\left(1 + \frac{M_{w,j}}{M_{w,i}}\right)]^{1/2}} \tag{10}$$

where, X_i is the mole fraction of the gas component. By the definition of Reynolds number, for a flow field inside a tube:

$$Re = \frac{\rho v d}{\mu} \tag{11}$$

where ρ represents the density of the gas mixture; v denotes the average velocity of the fluid; d is the pipe diameter in the fluid region; and μ is the coefficient of hydrodynamic viscosity.

To simplify the explanation of the calculation process, a schematic diagram (Figure S15) shows the connection between the inlet pipe with d=0.007 m and the quartz pipe with D=0.04 m. According to equation (9) and (10), the gas viscosity in the quartz pipe (D=0.04 m) is calculated to be 1.75×10^{-5} kg/m s and the density is 1.19 kg/m³. In the inlet pipe (d=0.007 m), the gas viscosity is 2.125×10^{-5} kg/m s and the density is 1.6633 kg/m³. Additionally, 120 sccm has been determined as the optimal carrier gas flow rate for investigating the effect of carrier gas velocity on the MoS_2 growth process. By dividing the volumetric flow rate by the cross-sectional area, the velocity in the quartz pipe (D=0.04 m) is calculated to be 0.002 m/s, and the velocity in the inlet pipe (d=0.007 m) is 0.05 m/s. After correction, the *Re* in the quartz pipe is recalculated to be 4.34, and in the inlet pipe, it is 28.5.

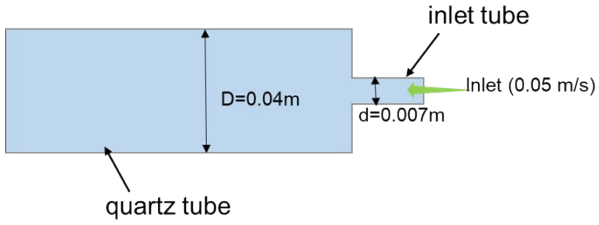

Figure S15. Schematic diagram of inlet pipe and quartz pipe connection section.

Impact of eddy currents on the Growth Process of MoS_2:

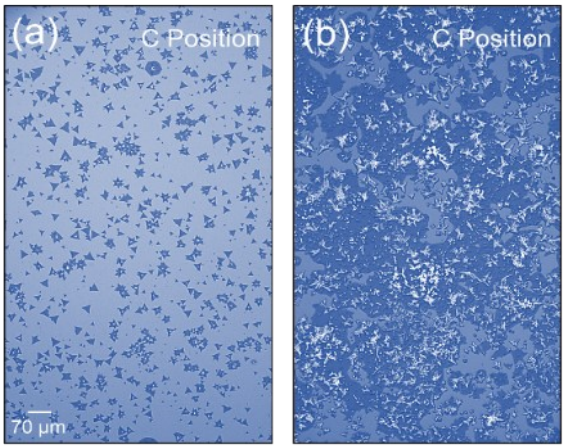

Figure S16. Growth results at position c upstream of the substrate at the same conditions with and without 2 mm gap. (a) Growth results with a 2 mm gap; (b) Growth results without 2 mm gap.

To verify the effect of maintaining a 2 mm gap between the substrate and the quartz boat, we conducted an additional MoS_2 growth experiment without this gap under the same conditions. We selected position c upstream of the substrate for observation of growth results, this position is closer to the interface between the substrate and the bottom of the quartz boat. The results are shown in Figure S16, where (a) represents the growth results with a 2 mm gap, and (b) represents the results without the gap.

It is evident that in Figure S16(b), MoS_2 tends to grow vertically, forming a thicker, dendritic morphology. Conversely, in the growth results with the gap, MoS_2 exhibits horizontal, epitaxial growth, resulting in a uniform monolayer. In the absence of the gap, eddy currents at the bottom of the substrate cause turbulence in the growth rate at position c, making it difficult to establish a stable MoS_2 growth environment, resulting in out-of-plane growth and the formation of MoS_2 dendrites[7,6,8,9]. In comparison,

under the condition with a 2 mm gap, the adverse effects of eddy currents are mitigated, fostering a stable environment that is favorable for forming a uniform monolayer of MoS_2[10,11].

Evaporation rate of S calculation:

During the experiment, 1 g of sulfur powder is placed in a quartz boat upstream of the substrate. Three minutes before the temperature reaches the optimal growth temperature, the quartz boat with the sulfur is pushed into the S zone, initiating the evaporation of the sulfur. The sulfuration growth process is then maintained for 20 minutes. Experimental results indicate that approximately 2 minutes after completing the sulfuration, the sulfur in the quartz boat is nearly fully evaporated, leading to an estimated total evaporation time of 25 minutes. The evaporation rate can be calculated from the total amount of evaporation divided by the evaporation time as 6.67×10^{-7} kg/s.

Detailed section of simulation calculations：

In the simulation, tetrahedral grids are employed for mesh generation to enhance smoothness, reduce computational costs, and preserve detailed features of the computational model. Meshes for the substrate and quartz boat are refined to accurately capture gradient changes and improve computational accuracy. Grid independence is verified by measuring the velocity values above the substrate, ensuring no significant changes with an increase in the number of grids. And, the obtained flow field is relatively

clear, with approximately 780,000 small grids used in our calculations.

In the simulation, the bottom surface of the quartz boat within the S-zone is designated as the diffusion surface for sulfur vapor, and defined as MASS_FLOW_INLET boundary condition. The inlet pipe is set as VELOCITY_INLET boundary condition, while the outlet pipe is set as OUTFLOW boundary condition. Both the front and rear ends of the pipe are designated as wall surfaces (WALL) for cold wall treatment. The Mo-zone and S-zone in the middle of the pipe are designated as hot wall surfaces, with the wall temperature set to 820 ℃ for the Mo-zone and 280 ℃ for the S-zone. No-slip boundary conditions are applied to all solid surfaces.

All the basic equations for CFD simulation are given below:

The equation for conservation of mass is:

$$\frac{\partial \rho}{\partial t} + \frac{\partial(\rho u)}{\partial x} + \frac{\partial(\rho v)}{\partial y} + \frac{\partial(\rho w)}{\partial z} = 0 \tag{12}$$

where u, v, and w are the velocity components in the x, y, and z directions in the right-angle coordinate system, respectively, and ρ is the density.

The equation for conservation of momentum is:

$$\frac{\partial u}{\partial t} + u\frac{\partial u}{\partial x} + v\frac{\partial u}{\partial y} + w\frac{\partial u}{\partial z} = -\frac{1\partial P}{\rho \partial x} + F_x + \frac{1}{\rho}\left(\frac{\partial \tau_{xx}}{\partial x} + \frac{\partial \tau_{xy}}{\partial y} + \frac{\partial \tau_{xz}}{\partial z}\right) \tag{13.1}$$

$$\frac{\partial v}{\partial t} + u\frac{\partial v}{\partial x} + v\frac{\partial v}{\partial y} + w\frac{\partial v}{\partial z} = -\frac{1\partial P}{\rho \partial y} + F_y + \frac{1}{\rho}\left(\frac{\partial \tau_{yx}}{\partial x} + \frac{\partial \tau_{yy}}{\partial y} + \frac{\partial \tau_{yz}}{\partial z}\right) \tag{13.2}$$

$$\frac{\partial w}{\partial t} + u\frac{\partial w}{\partial x} + v\frac{\partial w}{\partial y} + w\frac{\partial w}{\partial z} = -\frac{1\partial P}{\rho \partial z} + F_z + \frac{1}{\rho}\left(\frac{\partial \tau_{zx}}{\partial x} + \frac{\partial \tau_{zy}}{\partial y} + \frac{\partial \tau_{zz}}{\partial z}\right) \tag{13.3}$$

where P is the pressure, τ is the viscous stress of the viscous fluid, τ_{ij} is its tensor component on indices (i,j), F is the external force per unit mass of the fluid, and μ is the fluid viscosity coefficient.

The equation for conservation of energy is:

$$\rho c\frac{DT}{Dt} = \nabla \cdot (k\nabla T) + \emptyset \tag{14}$$

where c represents the specific heat of the fluid, and Φ denotes the dissipation function for incompressible flow.

component transport equations:

$$\nabla(\rho u Y_i) = -\nabla J_i \tag{15.1}$$

$$J_i = -\rho D_{i,j} \nabla Y_i \tag{15.2}$$

where Y_i is the mass fraction of each component, J_i is the diffusion flux, and D_{ij} is the binary diffusion coefficient.

The detailed schematic of the geometry constructed in Ansys for the CFD simulation is shown in Figure S17.

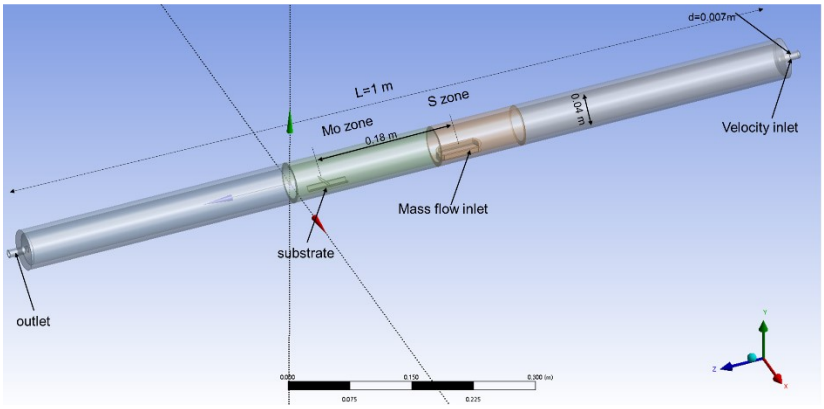

Figure S17. Detailed schematic of the geometric structure used in the simulation.

Calculating the Schmidt Number (*Sc*):

The practicality of boundary layer theory model depends on the ability to find an accurate and simple formula for δ. In this paper, we assume δ to be approximately 0.99 times δ_v. To validate this assumption, the Schmidt number (*Sc*) is utilized, linking the velocity boundary layer with the concentration boundary bounder. Specifically, when *Sc* approaches 1, the

rates of momentum and mass diffusion converge, supporting the assumption that the thickness of the velocity boundary layer is comparable to that of the concentration boundary layer. In previous discussions, we determined the diffusion coefficient of the gas mixture to be 1.26×10^{-5} (m^2/s), viscosity as 1.75×10^{-5} kg/m s, and density as 1.19 kg/m^3. Substituting these values into Equation (16) yields *S*c=1.16, which closely approximates 1. Therefore, we substantiate our assumption that δ is approximately 0.99 times δ_v.

$$S_c = \frac{\mu}{\rho D_{ij}} \tag{16}$$

References

1. Q. Wang, Q. Xu, J. Yin, H. Zhu, B. Liu and M. Yang, *Crystengcomm*, 2022, **24**, 3035-3048.
2. Q. Wang, Q. Xu, M. Yang, Z. Wu, X. Xia, J. Yin and Z. Han, *ACS Appl. Mater. Interfaces*, 2023, **15**, 17396-17405.
3. R. Somphonsane, T. Chiawchan, W. Bootsa-Ard and H. Ramamoorthy, *Materials*, 2023, **16**, 4817.
4. S. Yang, J. Wu, C. Wang, H. Yan, L. Han, J. Feng, B. Zhang, D. Li, G. Yu and B. Luo, *Dalton Trans.*, 2022, **51**, 13351-13360.
5. J. Xu and D. Ho, *Chem. Mat.*, 2021, **33**, 3249-3257.
6. W. Xu, S. Li, S. Zhou, J. K. Lee, S. Wang, S. G. Sarwat, X. Wang, H. Bhaskaran, M. Pasta and J. H. Warner, *ACS Appl. Mater. Interfaces*, 2018, **10**, 4630-4639.
7. T. Chiawchan, H. Ramamoorthy, K. Buapan and R. Somphonsane, *Nanomaterials*, 2021, **11**, 2642.
8. F. Chen, X. Jiang, J. Shao, B. Lu, L. Fu, S. Zhao and W. Su, *Crystengcomm*, 2021, **23**, 1345-1351.
9. S. Wang, Y. Rong, Y. Fan, M. Pacios, H. Bhaskaran, K. He and J. H. Warner, *Chem. Mat.*, 2014, **26**, 6371-6379.
10. L. Tang, T. Li, Y. Luo, S. Feng, Z. Cai, H. Zhang, B. Liu and H. Cheng, *ACS Nano*, 2020, **14**, 4646-4653.
11. P. K. Mohapatra, S. Deb, B. P. Singh, P. Vasa and S. Dhar, *Appl. Phys. Lett.*, 2016, **108**.